Letter

Chiral orbital texture in nonlinear electrical conduction

Suguru Okumura, Ryutaro Tanaka, and Daichi Hirobe
Department of Physics, Shizuoka University, Suruga, Shizuoka, 422-8529, Japan

(Received 29 March 2024; revised 11 June 2024; accepted 10 July 2024; published 22 July 2024)

Nonlinear electrical conduction primarily mediated by an orbital texture is observed in chiral semiconductor Te. We determine the enantiospecific sign of the nonlinear conductance and identify anomalies in its carrier-density dependence. Our findings, combined with the Boltzmann equation, are attributed to a chiral orbital texture, namely a chiral distribution of the orbital magnetic moment in reciprocal space. This study underscores the efficacy of nonlinear transport measurements in probing orbital-related effects, whose differentiation from spin counterparts is often demanding in the linear response regime of electron transport.

DOI: 10.1103/PhysRevB.110.L020407

Introduction. Magnetoresistance (MR) denotes a variation in electrical resistance in response to a magnetic field, a phenomenon ubiquitous not only in magnetically ordered conductors but also in nonmagnetic conductors. In conventional MR effects in nonmagnetic conductors, the resistance change depends solely on the strength of a magnetic field, irrespective of its polarity. However, this paradigm changes when the system breaks inversion symmetry, rendering it noncentrosymmetric. Such noncentrosymmetry can produce MR that varies bilinearly with both the magnetic field B and the electric current I [1,2]. This bilinear MR produces a voltage proportional to the product of I^2 and B, underscoring its nonlinearity and unipolar dependence on B. Due to the characteristics, bilinear MR is also referred to as nonreciprocal magnetotransport [3], bulk charge rectification [4], magnetochiral anisotropy [5,6], and unidirectional magnetoresistance [7]. This capability to rectify an electric current without the need for heterojunctions holds promise for utilizing noncentrosymmetric properties in electronics. For its direct relevance to our observables, we adopt the term nonlinear electrical conduction (NEC) in this paper to mean bilinear MR in noncentrosymmetric conductors lacking magnetic ordering and heterojunctions.

NEC can arise from several sources, including the Zeeman interaction [4,8] and the Berry curvature [9]. In the context of noncentrosymmetry, the spin texture in quasimomentum ($\boldsymbol{k}$) space is often emphasized. Notably, an orbital counterpart equally represents noncentrosymmetry without the need for spin-orbit coupling: the orbital magnetic moment of a Bloch electron in $\boldsymbol{k}$ space [10,11]. The orbital texture can be conceived as the $\boldsymbol{k}$-dependent self-rotation of a wavepacket about its center of mass in semiclassical theory. Theoretical predictions suggest that the orbital texture enables current-induced magnetization [12–14] and may even dominate over the spin texture in certain scenarios [15–17]. Recently, a similar theoretical argument has been applied to NEC, focusing on the three-dimensional chiral semiconductor Te [18]. Experimental indication of the relevance of the orbital magnetic moment near the Weyl points of Weyl semimetal WTe_2 was provided through the divergent behavior of magnetochiral anisotropy [9]. However, exploration of orbital-related nonlinear transport remains largely uncharted, raising the question of whether orbital-induced NEC is universal beyond materials exhibiting such topological singularities.

In this Letter, we report NEC induced primarily by a chiral orbital texture in p-type Te, where the chemical potential resides near the highest valence band without topological singularities. We confirm chirality-induced NEC in Te-based field-effect transistors, obeying the magnetic group of trigonal Te. Using symmetry-adapted selection rules, we determine a single component G_{zzzz} of the nonlinear electrical conductance tensor as a function of carrier density with high precision. The enantiospecific sign of G_{zzzz} is negative (positive) for right-handed (left-handed) Te, and G_{zzzz} exhibits a broad peak structure at low carrier densities. These characteristics are attributed primarily to a chiral orbital texture in $\boldsymbol{k}$ space, rather than the spin counterpart. This is rationalized by Boltzmann kinetic theory incorporating orbital and spin textures via the Zeeman interaction. Discriminating between orbital and spin contributions is often challenging in dynamical magnetoelectric effects. Our findings suggest that NEC measurements offer an effective means of probing elusive orbital textures across diverse materials.

Chiral properties of elemental tellurium. Trigonal Te is a p-type semiconductor with a narrow band gap of approximately 0.34 eV. Helical chains form along the c axis through covalent bonding of Te atoms, with adjacent chains interconnected via coordinate covalent bonding due to the multivalent nature of Te [19,20]. Consequently, Te crystallizes into enantiomorphic space groups, either $P3_121$ (right handed) or $P3_221$ (left handed) [Fig. 1(a)]. Numerous phenomena in Te are attributed to chirality, including hedgehoglike spin textures [21,22], optical activity [23–26], current-induced magnetization [27–30], asymmetric etch pits [31], NEC [32–35], second-harmonic generation [35–37], circular photogalvanic and photovoltaic effects [38], and diffraction with circularly polarized x-rays [39]. The simplicity of its chiral structure has facilitated theoretical calculations of chirality-related properties for decades [40–48]. For modeling energy dispersions and magnetic moments, we adopt the tight-binding model proposed in Ref. [48], wherein the reduced space is spanned by two conduction bands and four valence bands. Original parameters are

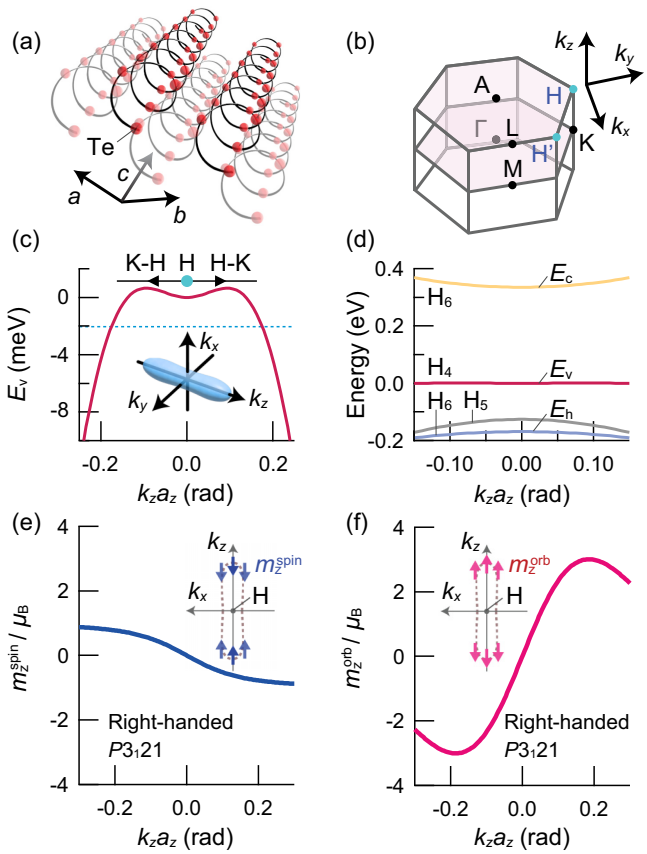

FIG. 1. (a) Crystal structure of right-handed Te of space group $P3_121$. (b) First Brillouin zone and representative highly symmetrical points. $k_{x,y,z}$ denote wavenumbers, measured from the H point. (c), (d) k_z dependences of the valence band E_v (c) and other bands located around E_v (d) in the vicinity of the H point. a_z is the lattice constant along the c axis. The Fermi surface of E_v at -2 meV is shown in (c). (e), (f) k_z dependences of the z components of the spin magnetic moment m_z^{spin} (e) and the orbital magnetic moment m_z^{orb} (f) for right-handed Te ($P3_121$).

adjusted to match *ab initio* calculations [47], which successfully reproduce experimentally confirmed enantiomeric spin magnetic moments [21,30]. The energy dispersion of the uppermost valence band near the H and H' points [Fig. 1(b)] is well approximated by $E_v(\boldsymbol{k}) = -\hbar^2/(2m_\perp^v)(k_x^2 + k_y^2) - \hbar^2/(2m_\parallel^v)k_z^2 + \sqrt{(Sk_z)^2 + \Delta^2} - \Delta$ [Fig. 1(c)], where $\hbar$ is the reduced Planck constant, and other parameter values are provided in the Supplemental Material [49] (see also Refs. [50–54] therein). The z and x axes are aligned with the c and a axes of Te, respectively. The spin magnetic moment $m_z^{spin}(\boldsymbol{k}) = \boldsymbol{m}^{spin}(\boldsymbol{k}) \cdot \boldsymbol{e}_z$ ($\boldsymbol{e}_z$: unit vector along the z axis) for $E_v(\boldsymbol{k})$ is represented by $m_z^{spin}(\boldsymbol{k}) = -\mu_B \eta(k_z)$, where $\eta(k_z) = Sk_z/\sqrt{(Sk_z)^2 + \Delta^2}$ and μ_B is the Bohr magneton. Crucially, the parameter S in $\eta(k_z)$ changes sign with the handedness of the lattice structure. Thus, $\boldsymbol{m}^{spin}(\boldsymbol{k})$ is handedness dependent and hedgehoglike in $\boldsymbol{k}$ space, which is a hallmark of chirality.

Such chirality is also evident in the orbital texture, even in the absence of spin-orbit coupling, in principle. The orbital magnetic moment $m_z^{orb}(\boldsymbol{k}) = \boldsymbol{m}^{orb}(\boldsymbol{k}) \cdot \boldsymbol{e}_z = -ie/(2\hbar)\langle \nabla_{\boldsymbol{k}} u_v| \times (H_{\boldsymbol{k}} - E_v(\boldsymbol{k}))|\nabla_{\boldsymbol{k}} u_v\rangle \cdot \boldsymbol{e}_z$ ($e > 0$: elementary charge) for the highest valence band can be approximated as [48]

$$m_z^{orb}(\boldsymbol{k}) = -\mu_B \left(\frac{\epsilon_c}{\Delta E_{vc}(\boldsymbol{k})} + \frac{\epsilon_h}{\Delta E_{vh}(\boldsymbol{k})} \right) \eta(k_z), \qquad (1)$$

with $\Delta E_{vc(vh)}(\boldsymbol{k}) = E_v(\boldsymbol{k}) - E_{c(h)}(\boldsymbol{k})$ denoting the energy difference between E_v and the highest conduction (lowest valence) band [see also Fig. 1(d)]. Here, $\epsilon_c = 4.965$ eV and $\epsilon_h = 1.745$ eV are parameters adjusted to match *ab initio* calculations [49]. As illustrated in Figs. 1(e) and 1(f), m_z^{orb} not only surpasses m_z^{spin} in magnitude but also exhibits the opposite sign. Moreover, the energy dependence of m_z^{orb} differs from that of m_z^{spin} due to a suppression for higher $\boldsymbol{k}$ [Fig. 1(f)], arising from the interband nature of the orbital magnetic moment [11]. These distinctive features of the orbital texture motivated us to explore the corresponding NEC.

Experimental details. Te slabs were synthesized with several modifications to the original protocol [49,55]: specifically, we reduced the amount of reducing agent in the hydrothermal synthesis and extended the reaction time approximately threefold to produce thicker Te slabs. These Te slabs exhibited NEC based on the three-dimensional magnetic group while retaining gate-variable resistances. The Te slabs were laminated on a SiO_2 dielectric (300 nm thick) atop the doped Si substrate [Fig. 2(a)]. Electrode patterns were defined using standard photolithography for three devices: devices A and B included two-terminal electrodes, while device C included Hall and four-terminal electrodes. Metal electrodes were deposited via electron beam evaporation, with a 20 nm thick layer of Ni followed by a 60 nm thick layer of Au for capping to prevent Ni oxidation. Ni was selected to suppress the energy band bending near the Te/electrode interface [56]. For voltage measurements, harmonic voltages were detected using phase-sensitive detection combined with pulse amplitude modulation to minimize the self-heating of devices. Electric current pulses were modulated in a regularly timed sequence, resulting in a sinusoidal waveform of the envelope $I(t) = \sqrt{2} I_{rms} \sin(2\pi f t)$, where t denotes time; f a frequency; I_{rms} a root mean square current. f was referenced for phase-sensitive detection of root mean square harmonic voltages V_{rms}^{1X} at f in phase with $I(t)$ and V_{rms}^{2Y} at $2f$ out of phase with $I(t)$. Note that uppercase X and Y denote phase relations in phase-sensitive detection, not Cartesian coordinates. All measurements were conducted in a custom-made cryostat under a vacuum level of approximately 1×10^{-5} Pa. Magnetic field up to 500 mT was applied by electromagnet. The space group of devices except device C was determined by observing asymmetric etch pits formed using hot sulfuric acid [Fig. 2(b)] before electrical measurements, with reference to Ref. [31].

Absolute sign of the nonlinear electrical conductance. In Figs. 2(c) and 2(d), we present the normalized second harmonic resistance, $\overline{R}_{zz}^{2Y} = V_{rms}^{2Y}/V_{rms}^{1X}$, as a function of the magnetic field B and I_{rms} at 50 K, both applied along the z axis. $\overline{R}_{zz}^{2Y}$ is B and I_{rms} linear for both enantiomers, consistent with bilinear MR. Notably, sign reversal of $\overline{R}_{zz}^{2Y}$ is observed between the two enantiomers. Further confirmation

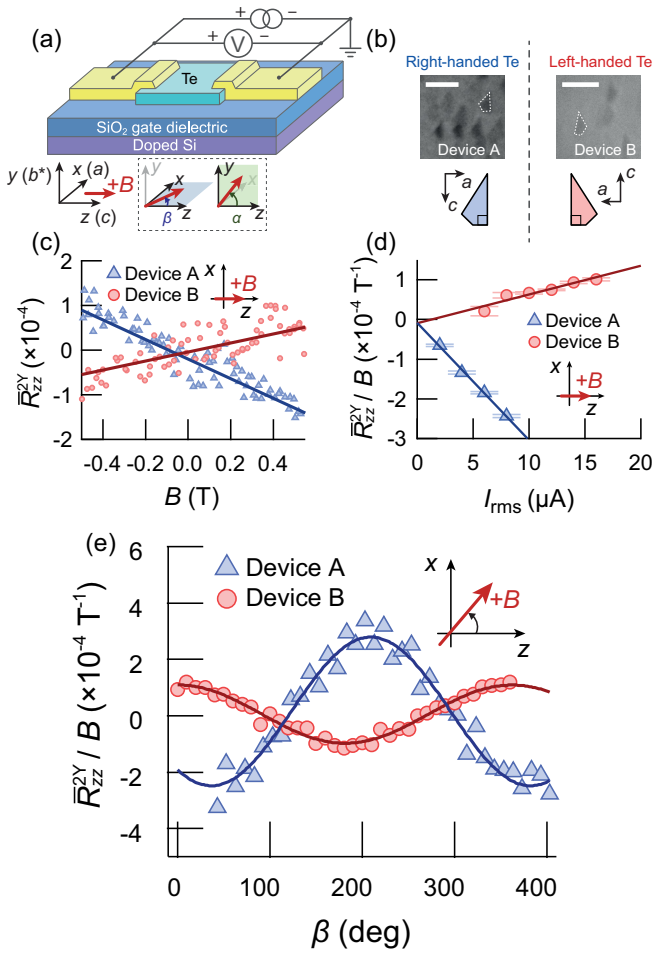

FIG. 2. (a) Schematic of the experimental setup for devices A and B. Magnetic field is denoted by B, and its angles by α in the yz plane and β in the zx plane. (b) Scanning electron microscope images of asymmetric etch pits formed on the $(10\bar{1}0)$ surface. Scale bar: 1 μm. (c), (d) Bilinear dependence of the normalized second harmonic resistance $\overline{R}_{zz}^{2Y}$ on B (c) and electric current $I_{\rm rms}$ (d), measured at 50 K. (e) β dependence of $\overline{R}_{zz}^{2Y}$. $I_{\rm rms}$ was set to 10 and 18 μA for devices A and B, respectively, in (c) and (e).

of chirality-induced NEC is provided by the dependence of the slope $\overline{R}_{zz}^{2Y}/B$ on the magnetic field angle, β, measured from the z axis in the zx plane [Fig. 2(e)]. $\overline{R}_{zz}^{2Y}/B$ collapses onto a single cosine wave for each enantiomer and exhibits sign reversal between the two enantiomers over the entire range of β. The observed behavior is fully consistent with the selection rule deduced from the magnetic group of trigonal Te. For Te thin films and nanowires, the dependence on β often deviated from $\cos\beta$ [32,35], complicating comparison with theoretical discussions on the origin of NEC.

We note that the absolute magnitude of $\overline{R}_{zz}^{2Y}/B$ was not the same between devices A and B at the same excitation current, which could be attributed to different charge rectification efficiencies due to different chemical-potential positions [18,33]. We found semiconducting and metallic behaviors for devices A and B, respectively, by temperature-variable harmonic resistance measurement [49]. Therefore, device A is expected to exhibit the higher rectification efficiency due to the higher chemical-potential position [18,33], which is consistent with the higher value of $\overline{R}_{zz}^{2Y}/B$. In addition, we confirmed that the absolute sign and magnitude of $\overline{R}_{zz}^{2Y}/B$ was consistent between two-terminal and four-terminal measurements using another device [49], which demonstrates the negligibly small contribution of contact resistance to NEC in our experiment.

Our results allow precise determination of a finite component G_{zzzz} of the nonlinear electrical conductance tensor. G_{zzzz} appears in a longitudinal electric current $I_z = G_{zz}V_z + G_{zzzz}(V_z)^2B_z + \mathcal{O}((V_z)^3, (B_z)^2)$, where I_z, V_z, and B_z denote z components of electric current, voltage, and magnetic field while G_{zz} denotes linear electrical conductance. Direct computation yields $\overline{R}_{zz}^{2Y} = 2^{-1/2}(G_{zz})^{-2}G_{zzzz}I_{\rm rms}B\cos\beta$ [49], enabling determination of G_{zzzz} by fitting to $\overline{R}_{zz}^{2Y}/B$ with $\cos\beta$. We find $G_{zzzz} = -14.5 \pm 0.6\ \mathrm{nAV^{-2}T^{-1}}$ for right-handed Te (device A) and $G_{zzzz} = 220 \pm 8\ \mathrm{nAV^{-2}T^{-1}}$ for left-handed Te (device B). The enantiospecific sign was double checked by d.c. magnetoconductance measurement [49].

We address the enantiospecific sign of G_{zzzz} based on orbital and spin textures, which has not been discussed in previous studies. We calculate the corresponding nonlinear electrical conductivity g_{zzzz} due to the Zeeman interaction for the energy dispersion $E_{\rm v}(\boldsymbol{k}) - \{m_z^{\rm orb}(\boldsymbol{k}) + m_z^{\rm spin}(\boldsymbol{k})\}B_z$, following the Boltzmann kinetic theory which accounts for elastic impurity scattering [57]. Because this energy band is separated from the second highest valence band and the lowest conduction band by about 1500 K and 4000 K at the H point, respectively, electrical conduction by those thermally inactive bands is ignored in the present calculation. In this framework, we express g_{zzzz} as the sum of orbital ($g_{zzzz}^{\rm orb}$) and spin ($g_{zzzz}^{\rm spin}$) parts, and $g_{zzzz}^{\rm orb}$ is given by [49]

$$g_{zzzz}^{\rm orb} = \int \frac{d\boldsymbol{k}}{(2\pi)^3}\mathfrak{g}_{zzzz}^{\rm orb}(\boldsymbol{k})\left(-\frac{\partial f_0}{\partial E}\right)\bigg|_{E=E_{\rm v}}, \tag{2}$$

where $\mathfrak{g}_{zzzz}^{\rm orb}(\boldsymbol{k}) = -(2e^3/5\hbar^2)\tau_{\boldsymbol{k}}^2\partial_{k_z}[v_z^2\partial_{k_z}(m_z^{\rm orb}/v_z)]$. Here, $v_z = (1/\hbar)\partial_{k_z}E_{\rm v}$, and $f_0(E)$ denotes the Fermi-Dirac distribution function for electrons. $\tau_{\boldsymbol{k}}$ represents an effective relaxation time for NEC [49]. $g_{zzzz}^{\rm spin}$ is determined in the same way. We focus on the absolute sign by considering $\mathfrak{g}_{zzzz}^{\rm orb,spin}(\boldsymbol{k})$ in the k_z-k_x plane for left-handed Te [Figs. 3(a) and 3(b)]. $\mathfrak{g}_{zzzz}^{\rm orb}$ is positive while $\mathfrak{g}_{zzzz}^{\rm spin}$ is negative, originating from the opposite signs of $m_z^{\rm orb}$ and $m_z^{\rm spin}$. Notably, the sum $\mathfrak{g}_{zzzz} = \mathfrak{g}_{zzzz}^{\rm orb} + \mathfrak{g}_{zzzz}^{\rm spin}$ is positive over the entire $\boldsymbol{k}$ space around the H point [Fig. 3(c)], resulting in a positive sign of g_{zzzz} within the accessible energy range of our measurement: the same sign as left-handed $G_{zzzz} > 0$. Because the orbital and spin textures change sign with the handedness of Te, the present argument holds equally for right-handed $G_{zzzz} < 0$. The agreement in enantiospecific sign demonstrates that NEC primarily originates from the orbital texture. Contributions of the Berry curvature ($\mathfrak{g}_{zzzz}^{\rm BC}$) were not considered in the calculations. Boltzmann kinetic theory combined with *ab initio* calculations [18] showed that $\mathfrak{g}_{zzzz}^{\rm BC}$ is even smaller than $\mathfrak{g}_{zzzz}^{\rm spin}$, because $\mathfrak{g}_{zzzz}^{\rm BC}$ is directly proportional to the low group velocity, unlike $\mathfrak{g}_{zzzz}$, alongside the absence of topological singularities.

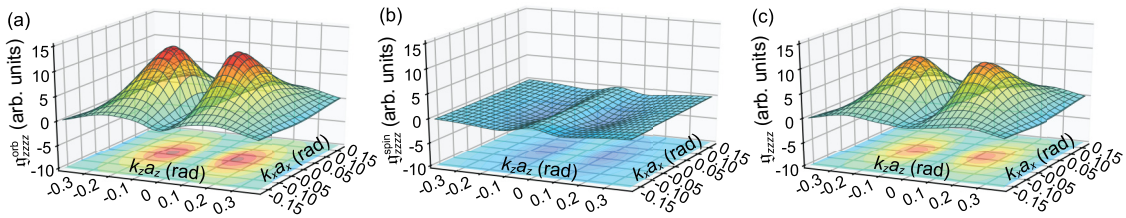

FIG. 3. (a)–(c) $\boldsymbol{k}$-resolved nonlinear conductivity of left-handed Te for orbital $\mathfrak{g}^{\rm orb}_{zzzz}$ (a), spin $\mathfrak{g}^{\rm spin}_{zzzz}$ (b), and their sum $\mathfrak{g}_{zzzz}$ (c).

Carrier density dependence of G_{zzzz}. To investigate the carrier-density dependence of G_{zzzz}, we fabricated a Te crystal into a field-effect transistor [device C in Fig. 4(a)], where longitudinal and Hall voltages were measured to calculate G_{zzzz} and the sheet carrier density $n_{\rm S}$ at various bottom-gate voltages. By varying the magnetic field angle α in the yz plane, we were able to precisely determine G_{zzzz} and $n_{\rm S}$ by fitting with $\cos\alpha$ and $\sin\alpha$, respectively, as illustrated in Fig. 4(b).

The dependence of G_{zzzz} on $n_{\rm S}$ is shown in Fig. 4(c). G_{zzzz} decreases with decreasing $n_{\rm S}$ at a temperature T of 20 K, which is the lowest temperature of our measurement system. However, the magnitude of the slope decreases below $n_{\rm S} \sim 17 \times 10^{12}\,{\rm cm}^{-2}$ and increases again below $n_{\rm S} \sim 8 \times 10^{12}\,{\rm cm}^{-2}$. Consequently, G_{zzzz} exhibits a broad peak structure in the low carrier density range. This peak structure weakens and disappears with increasing T. Figure 4(d) demonstrates that these observed trends are consistent with calculated g_{zzzz}, where the chemical potential and temperature were considered via $f_0(E)$. Division of g_{zzzz} into $g^{\rm orb}_{zzzz}$ and $g^{\rm spin}_{zzzz}$ reveals that the peak structure is primarily caused by $g^{\rm orb}_{zzzz}$ rather than $g^{\rm spin}_{zzzz}$ in the carrier-density dependence [see the inset to Fig. 4(d)]. Therefore, our findings suggest that G_{zzzz} reflects the energy dependence of $m^{\rm orb}_z$ embedded in $g^{\rm orb}_{zzzz}$, which is concentrated around the valence band top (see also Fig. 1). Within the present temperature range, charge carriers experience non-negligible scattering due to electron-phonon and electron-electron interactions, not accounted for in our calculations based on elastic impurity scattering. Consequently, the calculated carrier-density dependence of NEC would be less apparent in experiments, possibly due to Matthiessen's rule of the relaxation times.

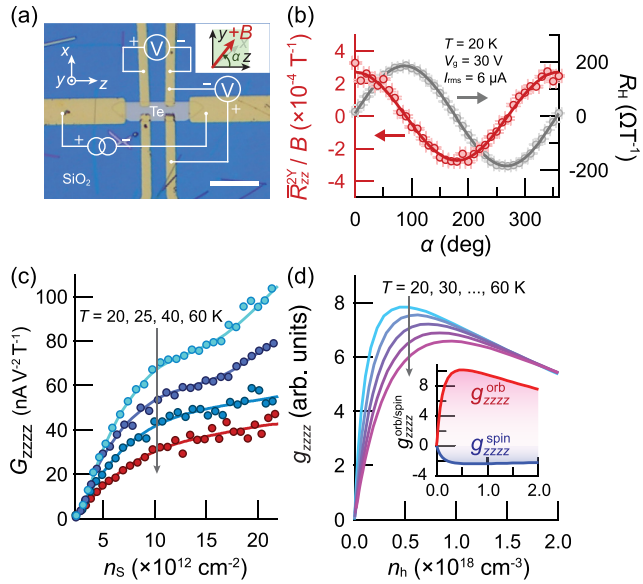

FIG. 4. (a) Microscope image of device C. Scale bar: 30 μm. (b) Dependences of $\overline{R}^{2Y}_{zz}$ and the Hall coefficient $R_{\rm H}$ on α, measured at back gate voltage $V_{\rm g} = 30$ V and temperature $T = 20$ K. (c) Nonlinear conductance G_{zzzz} as a function of the sheet carrier density $n_{\rm S}$. Lines are guides to the eye. (d) Nonlinear conductivity g_{zzzz} as a function of the hole carrier density $n_{\rm h}$. The orbital component $g^{\rm orb}_{zzzz}$ and the spin component $g^{\rm spin}_{zzzz}$ at 20 K are also shown in the inset.

Our calculations did not consider the extrinsic orbital magnetic moment $\boldsymbol{m}^{\rm orb,ext}$, arising from the antisymmetric impurity scattering [48]. Because scattering processes responsible for $m^{\rm orb,ext}_z = \boldsymbol{m}^{\rm orb,ext} \cdot \boldsymbol{e}_z$ are enhanced with increasing $k_{x,y}$, $m^{\rm orb,ext}_z$ is enhanced with increasing carrier density or expanding Fermi surface. Theoretically, the current-induced orbital magnetization of Te changes from intrinsic to extrinsic with increasing carrier density, and a similar carrier-density dependence to Fig. 4(c) is exhibited by the conversion efficiency [48]. The crossover may be relevant to our results, explaining the monotonic increase of G_{zzzz} for higher $n_{\rm S}$. Even for this mechanism, there exists a low carrier density range in which $k_{x,y}$ is much smaller than k_z, and NEC discernibly derives from the orbital magnetic moment determined by the band structure. We interpret the observed broad peak structure as an indication of such a carrier density range.

Summary. We investigated the nonlinear electrical conduction (NEC) in chiral semiconductor Te, and uncovered that NEC primarily stems from the chiral orbital texture of a Bloch electron. This was evidenced by the enantiospecific sign of the nonlinear electrical conductance and anomalies in its carrier-density dependence. These experimental characteristics were rationalized by integrating semiclassical Boltzmann kinetic theory, accounting for the orbital texture via the Zeeman interaction. Our findings underscore the crucial role of orbital effects in inducing NEC and highlight the potential of NEC measurements in probing orbital textures across various materials.

Note added. Immediately before submitting the original version of our manuscript, we became aware of the theoretical work by Nakazawa *et al.* based on *ab initio* calculations [58], who calculated another type of nonlinear charge transport driven by the product of the electric field and the temperature gradient. They identified the orbital magnetic moment as the primary origin of this effect in the vicinity of the valence band top.

Acknowledgments. We thank T. Seki for technical assistance in sulfuric acid etching. We are also grateful to M. Matsumoto for his discussions. We acknowledge T. Mieno for the support of scanning electron microscopy provided by Molecular Structure Analysis Section, Shizuoka Instrumental Analysis Center, Shizuoka University. This work was supported by Grant-in-Aid for Scientific Research (B) (23H01836), for Challenging Research (Exploratory) (22K18695, 24K21527), and for Transformative Research Areas (A) (24H02234) from JSPS KAKENHI, Japan as well as PRESTO "Topological Materials Science for Creation of Innovative Functions" (JPMJPR20L9) from Japan Science and Technology Agency, Japan.

[1] G. L. J. A. Rikken, J. Fölling, and P. Wyder, Electrical magnetochiral anisotropy, Phys. Rev. Lett. **87**, 236602 (2001).
[2] G. L. J. A. Rikken and P. Wyder, Magnetoelectric anisotropy in diffusive transport, Phys. Rev. Lett. **94**, 016601 (2005).
[3] Y. Tokura and N. Nagaosa, Nonreciprocal responses from noncentrosymmetric quantum materials, Nat. Commun. **9**, 3740 (2018).
[4] T. Ideue, K. Hamamoto, S. Koshikawa, M. Ezawa, S. Shimizu, Y. Kaneko, Y. Tokura, N. Nagaosa, and Y. Iwasa, Bulk rectification effect in a polar semiconductor, Nat. Phys. **13**, 578 (2017).
[5] F. Pop, P. Auban-Senzier, E. Canadell, G. L. J. A. Rikken, and N. Avarvari, Electrical magnetochiral anisotropy in a bulk chiral molecular conductor, Nat. Commun. **5**, 3757 (2014).
[6] T. Yokouchi, N. Kanazawa, A. Kikkawa, D. Morikawa, K. Shibata, T. Arima, Y. Taguchi, F. Kagawa, and Y. Tokura, Electrical magnetochiral effect induced by chiral spin fluctuations, Nat. Commun. **8**, 866 (2017).
[7] C. Avci, K. Garello, A. Ghosh, M. Gabureac, S. F. Alvarado, and P. Gambardella, Unidirectional spin Hall magnetoresistance in ferromagnet/normal metal bilayers, Nat. Phys. **11**, 570 (2015).
[8] P. He, C.-H. Hsu, S. Shi, K. Cai, J. Wang, Q. Wang, G. Eda, H. Lin, V. Pereira, and H. Yang, Nonlinear magnetotransport shaped by Fermi surface topology and convexity, Nat. Commun. **10**, 1290 (2019).
[9] T. Yokouchi, Y. Ikeda, T. Morimoto, and Y. Shiomi, Giant magnetochiral anisotropi in Weyl semimetal WTe_2 induced by diverging Berry Curvature, Phys. Rev. Lett. **130**, 136301 (2023).
[10] M.-C. Chang and Q. Niu, Berry phase, hyperorbits, and the Hofstadter spectrum: Semiclassical dynamics in magnetic Bloch bands, Phys. Rev. B **53**, 7010 (1996).
[11] D. Xiao, M.-C. Chang, and Q. Niu, Berry phase effects on electronic properties, Rev. Mod. Phys. **82**, 1959 (2010).
[12] T. Yoda, Y. Yokoyama, and S. Murakami, Current-induced orbital and spin magnetizations in crystals with helical structure, Sci. Rep. **5**, 12024 (2015).
[13] S. Zhong, J. E. Moore, and I. Souza, Current-induced orbital and spin magnetizations in crystals with helical structure, Phys. Rev. Lett. **116**, 077201 (2016).
[14] T. Yoda, Y. Yokoyama, and S. Murakami, Orbital Edelstein effect as a condensed-matter analog of solenoids, Nano Lett. **18**, 916 (2018).
[15] W.-Y. He, D. Goldhaber-Gordon, and K. T. Law, Giant orbital magnetoelectric effect and current-induced magnetization switching in twisted bilayer graphene, Nat. Commun. **11**, 1650 (2020).
[16] W.-Y. He and K. T. Law, Superconducting orbital magnetoelectric effect and its evolution across the superconductor-normal metal phase transition, Phys. Rev. Res. **3**, L032012 (2021).
[17] L. Chirolli, M. T. Mercaldo, C. Guarcello, F. Giazotto, and M. Cuoco, Colossal orbital Edelstein effect in noncentrosymmetric superconductors, Phys. Rev. Lett. **128**, 217703 (2022).
[18] X. Liu, I. Souza, and S. S. Tsirkin, Electrical magnetochiral anisotropy in trigonal tellurium from first principles, arXiv:2303.10164.
[19] Z. Zhu, X. Cai, S. Yi, J. Chen, Y. Dai, C. Niu, Z. Guo, M. Xie, F. Liu, J.-H. Cho, Y. Jia, and Z. Zhang, Multivalency-driven formation of Te-based monolayer materials: A combined first-principles and experimental study, Phys. Rev. Lett. **119**, 106101 (2017).
[20] S. Yi, Z. Zhu, X. Cai, Y. Jia, and J.-H. Cho, The nature of bonding in bulk tellurium composed of one-dimensional helical chains, Inorg. Chem. **57**, 5083 (2018).
[21] M. Sakano, M. Hirayama, T. Takahashi, S. Akebi, M. Nakayama, K. Kuroda, K. Taguchi, T. Yoshikawa, K. Miyamoto, T. Okuda, K. Ono, H. Kumigashira, T. Ideue, Y. Iwasa, N. Mitsuishi, K. Ishizaka, S. Shin, T. Miyake, S. Murakami, T. Sasagawa *et al.*, Radial spin texture in elemental tellurium with chiral crystal structure, Phys. Rev. Lett. **124**, 136404 (2020).
[22] G. Gatti, D. Gosálbez-Martínez, S. S. Tsirkin, M. Fanciulli, M. Puppin, S. Polishchuk, S. Moser, L. Testa, E. Martino, S. Roth, P. Bugnon, L. Moreschini, A. Bostwick, C. Jozwiak, E. Rotenberg, G. D. Santo, L. Petaccia, I. Vobornik, J. Fujii, J. Wong *et al.*, Radial spin texture of the Weyl fermions in chiral tellurium, Phys. Rev. Lett. **125**, 216402 (2020).
[23] K. C. Nomura, Optical activity in tellurium, Phys. Rev. Lett. **5**, 500 (1960).
[24] S. Fukuda, T. Shiosaki, and A. Kawabata, Infrared optical activity in tellurium, Physica Status Solidi (b) **68**, K107 (1975).
[25] S. Ades and C. H. Champness, Optical activity of tellurium to 20 μm, J. Opt. Soc. Am. **65**, 217 (1975).
[26] H. Stolze, M. Lutz, and P. Grosse, The optical activity of tellurium, Physica Status Solidi (b) **82**, 457 (1977).
[27] L. E. Vorob'ev, E. L. Ivchenko, G. E. Pikus, I. I. Farbshtein, V. A. Shalygin, and A. V. Shturbin, Optical activity in tellurium induced by a current, JETP Lett. **29**, 441 (1979).
[28] V. A. Shalygin, A. N. Sofronov, L. E. Vorob'ev, and I. I. Farbshtein, Current-induced spin polarization of holes in tellurium, Phys. Solid State **54**, 2362 (2012).
[29] T. Furukawa, Y. Shimokawa, K. Kobayashi, and T. Itou, Observation of current-induced bulk magnetization in elemental tellurium, Nat. Commun. **8**, 954 (2017).
[30] T. Furukawa, Y. Watanabe, N. Ogasawara, K. Kobayashi, and T. Itou, Current-induced magnetization caused by crystal chirality

in nonmagnetic elemental tellurium, Phys. Rev. Res. **3**, 023111 (2021).

[31] A. Koma and S. Tanaka, Etch pits and crystal structure of tellurium, Physica Status Solidi (b) **40**, 239 (1970).

[32] F. Calavalle, M. Suárez-Rodríguez, B. Martín-García, A. Johansson, D. C. Vaz, H. Yang, I. V. Maznichenko, S. Ostanin, A. Mateo-Alonso, A. Chuvilin, I. Mertig, M. Gobbi, F. Casanova, and L. E. Hueso, Gate-tuneable and chirality-dependent charge-to-spin conversion in tellurium nanowires, Nat. Mater. **21**, 526 (2022).

[33] D. Hirobe, Y. Nabei, and H. M. Yamamoto, Chirality-induced intrinsic charge rectification in a tellurium-based field-effect transistor, Phys. Rev. B **106**, L220403 (2022).

[34] K. Sudo, Y. Yanagi, T. Takahashi, K.-K. Huynh, K. Tanigaki, K. Kobayashi, M.-T. Suzuki, and M. Kimata, Valley polarization dependence of nonreciprocal transport in a chiral semiconductor, Phys. Rev. B **108**, 125137 (2023).

[35] C. Niu, G. Qiu, Y. Wang, P. Tan, M. Wang, J. Jian, H. Wang, W. Wu, and P. D. Ye, Tunable chirality-dependent nonlinear electrical responses in 2D tellurium, Nano Lett. **23**, 8445 (2023).

[36] M. Cheng, S. Wu, Z.-Z. Zhu, and G.-Y. Guo, Large second-harmonic generation and linear electro-optic effect in trigonal selenium and tellurium, Phys. Rev. B **100**, 035202 (2019).

[37] Q. Fu, X. Cong, X. Xu, S. Zhu, X. Zhao, S. Liu, B. Yao, M. Xu, Y. Deng, C. Zhu *et al.*, Berry curvature dipole induced giant mid-infrared second-harmonic generation in 2D Weyl semiconductor, Adv. Mater. **35**, 2306330 (2023).

[38] C. Niu, S. Huang, N. Ghosh, P. Tan, M. Wang, W. Wu, X. Xu, and P. D. Ye, Tunable circular photogalvanic and photovoltaic effect in 2D tellurium with different chirality, Nano Lett. **23**, 3599 (2023).

[39] Y. Tanaka, S. P. Collins, S. W. Lovesey, M. Matsumami, T. Moriwaki, and S. Shin, Determination of the absolute chirality of tellurium using resonant diffraction with circularly polarized x-rays, J. Phys.: Condens. Matter **22**, 122201 (2010).

[40] O. Betbeder-Matibet and M. Hulin, A semi-empirical model for the valence band structure of tellurium, Physica Status Solidi (b) **36**, 573 (1969).

[41] T. Doi, K.Nakao, and H.Kamimura, The valence band structure of tellurium. I. The $k \cdot p$ perturbation method, J. Phys. Soc. Jpn. **28**, 36 (1970).

[42] J. Joannopoulos, M. Schlüter, and M. L. Cohen, Electronic structure of trigonal and amorphous Se and Te, Phys. Rev. B **11**, 2186 (1975).

[43] R. H. Asendorf, Space group of tellurium and selenium, J. Chem. Phys. **27**, 11 (1957).

[44] M. Hirayama, R. Okugawa, S. Ishibashi, S. Murakami, and T. Miyake, Weyl node and spin texture in trigonal tellurium and selenium, Phys. Rev. Lett. **114**, 206401 (2015).

[45] H. Peng, N. Kioussis, and G. J. Snyder, Elemental tellurium as a chiral *p*-type thermoelectric material, Phys. Rev. B **89**, 195206 (2014).

[46] E. L. Ivchenko and G. E. Pikus, New photogalvanic effect in gyrotropic crystals, JETP Lett. **27**, 604 (1978).

[47] S. S. Tsirkin, P. A. Puente, and I. Souza, Gyrotropic effects in trigonal tellurium studied from first principles, Phys. Rev. B **97**, 035158 (2018).

[48] C. Şahin, J. Rou, J. Ma, and D. A. Pesin, Pancharatnam-Berry phase and kinetic magnetoelectric effect in trigonal tellurium, Phys. Rev. B **97**, 205206 (2018).

[49] See Supplemental Material at http://link.aps.org/supplemental/10.1103/PhysRevB.110.L020407 for parameters used in the tight-binding model; details of hydrothermal synthesis and lamination of Te crystals; details of the etching method and scanning electron microscope images of etch pits over wide area; temperature-variable harmonic resistances of devices A and B; comparison between four- and two-terminal measurements of nonlinear electrical conduction; expression for the normalized second harmonic resistance in terms of linear and nonlinear electrical conductances; double checking of the sign of the nonlinear electrical conductance by d.c. magnetoconductance measurement; calculation of the nonlinear electrical conductivity by Boltzmann kinetic equation; and comparison of calculated carrier-density dependences of the nonlinear conductances due to orbital and spin magnetic moments, which are reconstructed from the inset to Fig. 4(d). It also contains Refs. [50–54].

[50] J. Schliemann and D. Loss, Anisotropic transport in a two-dimensional electron gas in the presence of spin-orbit coupling, Phys. Rev. B **68**, 165311 (2003).

[51] K. Výborný, A. A. Kovalev, J. Sinova, and T. Jungwirth, Semiclassical framework for the calculation of transport anisotropies, Phys. Rev. B **79**, 045427 (2009).

[52] Y. Liu, T. Low, and P. P. Ruden, Mobility anisotropy in monolayer black phosphorus due to scattering by charged impurities, Phys. Rev. B **93**, 165402 (2016).

[53] C. Xiao, D. Li, and Z. Ma, Unconventional thermoelectric behaviors and enhancement of figure of merit in Rashba spintronic systems, Phys. Rev. B **93**, 075150 (2016).

[54] S. Kim, S. Woo, and H. Min, Vertex corrections to the dc conductivity in anisotropic multiband systems, Phys. Rev. B **99**, 165107 (2019).

[55] Y. Wang III, G. Qiu, R. Wang, S. Huang, Q. Wang, Y. Liu, Y. Du, W. A. G., III, M. J. Kim, X. Xu, P. D. Ye, and W. Wu, Field-effect transistors made from solution-grown two-dimensional tellurene, Nat. Electron. **1**, 228 (2018).

[56] G. Qiu, S. Huang, M. Segovia, P. K. Venuthurumilli, Y. Wang, W. Wu, X. Xu, and P. D. Ye, Thermoelectric performance of 2D tellurium with accumulation contacts, Nano Lett. **19**, 1955 (2019).

[57] L. E. Golub, E. L. Ivchenko, and B. Spivak, Electrical magnetochiral current in tellurium, Phys. Rev. B **108**, 245202 (2023).

[58] K. Nakazawa, T. Yamaguchi, and A. Yamakage, Nonlinear charge transport properties in chiral tellurium, arXiv:2403.10337.